TUDelft

Delft University of Technology

Infrared thermography
philosophy, approaches, analysis—processing, and guidelines

Shrestha, Ranjit; Moradi, Morteza; Sfarra, Stefano; Kim, Wontae

Important note
To cite this publication, please use the final published version (if applicable).
Please check the document version above.

CHAPTER 10

Infrared thermography: philosophy, approaches, analysis—processing, and guidelines

Ranjit Shrestha[1], Morteza Moradi[2,3], Stefano Sfarra[4] and Wontae Kim[5]

[1]Department of Mechanical Engineering, School of Engineering, Kathmandu University, Dhulikhel, Kavrepalanchok, Nepal
[2]Structural Integrity & Composites Group, Aerospace Engineering Faculty, Delft University of Technology, Delft, The Netherlands
[3]Center of Excellence in Artificial Intelligence for Structures, Prognostics & Health Management, Aerospace Engineering Faculty, Delft University of Technology, Kluyverweg 1, Delft, The Netherlands
[4]Department of Industrial and Information Engineering and Economics (DIIIE), University of L'Aquila, L'Aquila, Italy
[5]Eco-Sustainable Energy Research Institute, Kongju National University, Seobuk-gu, Cheonan-si, Republic of Korea

10.1 Introduction

10.1.1 Infrared thermography

The first "Image of Heat" was produced in 1840 by Sir John Herschel [1]. Sir John was also able to show a primitive heat image in his study, which he called thermography.

Infrared was discovered between 1900 and 1920. Numerous patents were granted for devices that can detect people, artillery, airplanes, ships, and even icebergs. In particular, the earliest operating system was developed during World War I, whereas, in the interwar period, two revolutionary new infrared detectors were built, namely, the image converter and the photon detector [2].

The tactical military disadvantages of the so-called "active" thermal imaging systems provided the opportunity, after World War II, for further military–secret infrared research aimed at developing "passive" systems. It was only in the mid-1950s that thermal imaging devices began to be available to science and industry.

Recently, governments and airport security used infrared thermography (IRT) to detect suspected swine flu and other viral diseases during

both the 2009 and 2020 pandemic emergencies [3]. The use of IRT has increased dramatically in recent years in several sectors.

In modern thermographic cameras, the live thermogram reveals temperature variations very clearly,thanks to the use of innovative algorithms [4]. A demonstration is provided in this chapter.

10.1.2 Basic principle

IRT utilizes an infrared (thermal) camera to extract and analyze a thermal pattern based on the principle that each body at a temperature above absolute zero (−273.15°C) emits electromagnetic (EM) radiation. The EM radiation emitted by an object is sensed by the infrared camera and transformed into an electronic signal, which is then processed to produce a thermal image.

10.1.2.1 Basic infrared radiation

Fig. 10.1 shows an overview of the EM spectrum. Within the EM, infrared radiation occurs at frequencies above those of microwaves and just below those of red visible light (VL). The infrared band lies between 0.74 and 1000 µm of the EM spectrum and is divided into five parts: near-infrared (NIR) lying between 0.74 and 1 µm, short wavelength infrared (SWIR) lying between 1 and 3 µm, medium wavelength infrared (MWIR) lying between 3 and 5 µm, long wavelength infrared (LWIR) lying between 8 and 14 µm, and very long wavelength infrared which lies between 14 and 1000 µm. SWIR, MWIR, and LWIR are the regions where infrared imaging devices exist [5].
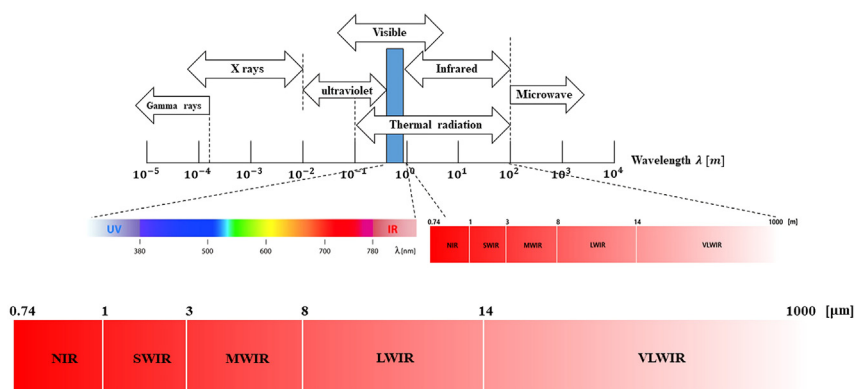

Figure 10.1 Electromagnetic spectrum with different infrared bands.

10.1.2.2 Radiation laws of the black body

A blackbody is a theoretical or model body that absorbs all radiation falling on it, reflecting or transmitting none. It is a hypothetical object that is a "perfect" absorber and "perfect" emitter of radiation at all wavelengths. The characteristics of blackbody radiation are explained with the help of Planck's law, Wien's displacement law, and Stefan—Boltzmann law.

Planck's law describes the spectral distribution of radiation emitted by a black body and can be expressed by Eq. (10.1) [6]. Fig. 10.2 depicts the graphic representation of a series of blackbody spectra for various temperatures following Eq. (10.1):

$$E_{\lambda,b}(\lambda, T) = \frac{C_1}{\lambda^5 \left(e^{\frac{C_2}{\lambda T}} - 1 \right)} \qquad (10.1)$$

where $E_{\lambda,b}$[W/m^2 μm] is the blackbody spectral radiant emittance at wavelength λ [μm] and temperature T [K], $C_1 = 2\pi hc = 3.742 \times 10^8$
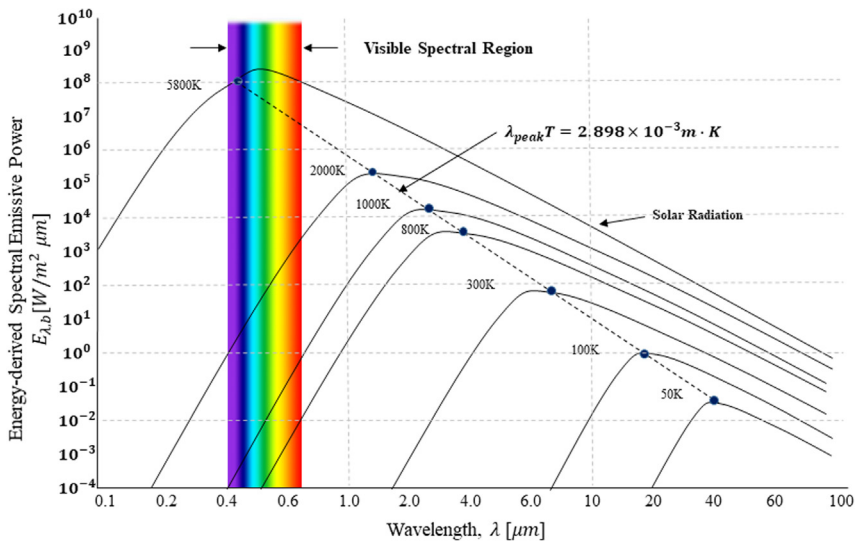
Figure 10.2 Spectral distribution of the radiation intensity from a blackbody according to Planck's law, plotted for various absolute temperatures. The dotted line represents the maximum radiant emittance points at each temperature according to Wien's Displacement Law. The maximum intensity of radiation emitted is within the infrared spectral band with the material under study at the temperatures it is usually found. Hence the cameras are sensitive to the infrared spectrum to measure the temperature, in addition to the atmospheric absorption is minimal between the body emitting radiation and the camera reading the emitted radiation.

[W $\mu m^4/m^2$] is the first radiation constant, and $C_2 = \frac{hc}{k} = 1.439 \times 10^4$ [μm K] is the second radiation constant, with $c = 2.998 \times 10^8$ [m/s] being the velocity of light in vacuum, $h = 6.626 \times 10^{-34}$ [J s] and $k = 1.381 \times 10^{-23}$ [J/K] the universal Planck and Boltzmann constants, respectively.

Wien's Displacement Law states that "The wavelength of the maximum intensity of blackbody radiation is inversely proportional to the temperature [7]." Graphically, this is represented in Fig. 10.2 and marked as a straight dotted line. It is found that the peak energy is proportional to their corresponding λ for varying temperatures and can be expressed by Eq. (10.2):

$$\lambda_{max} = \frac{C_3}{T} \tag{10.2}$$

where $C_3 = 2897.8$ [μm K] is the third radiation constant.

The Stefan−Boltzmann law can be obtained by integrating Planck's law over the entire spectrum ($0 < \lambda < \infty$) which states that "The total flux density Eb [W/m^2] emitted by a black body is proportional to the fourth power of its absolute temperature T" [7]. It can be expressed by Eq. (10.3):

$$E_b = \sigma T^4 \tag{10.3}$$

where $\sigma = 5.6697 \times 10^{-8}$ [W/m^2 K^4] denotes the Stefan−Boltzmann constant, which depends on C_1 and C_2 values.

10.1.2.3 Radiation laws of the real body

Objects in the real world are not perfect black bodies. Not all the incident energy upon them is absorbed; therefore, they are not perfect emitters of radiation. A real generic object may have a different ability to absorb (emit), reflect, and transmit energy concerning the black body owing to its bulk material nature and surface finishing, which can be expressed by Eq. (10.4) [7]:

$$\alpha + \rho + \tau = 1 \tag{10.4}$$

which links the total absorptance (α) to the total reflectance (ρ) and the total transmittance (τ).

10.1.2.4 Heat transfer mechanism

Heat transfer is the process of transferring heat from a high-temperature medium to a low-temperature medium. It is an essential tool that explains abnormal surface temperature patterns. The three heat transfer mechanisms are conduction, convection, and radiation. When dealing with transient thermal problems and inspection using IRT, conduction is the most important heat transfer mode, as this mechanism defines the amount of heat reached and finally emitted by the surface of the solid. Different materials conduct heat at different rates, and these rates are related to their thermal properties. The main thermophysical properties related to IRT are thermal conductivity, density, specific heat, diffusivity, and effusivity.

10.1.3 Thermography approaches

There are two approaches in thermography, that is passive and active thermography, which will be discussed in detail later. Moreover, defects can be active or passive. Passive defects are at the same temperature as the surrounding environment and hence need to be heated or cooled to produce defect indications. Whereas active defects emit or absorb thermal energy and can be detected in a passive mode [8].

10.1.3.1 Passive thermography

There is no extraneous energy required in passive thermography to stimulate a gradient of temperature at the structure or material being investigated. The aspects of importance are inherently below or above ambient temperature due to the object's self-heating or friction. This approach works well in two spectral regions, 3–5 m (MWIR) and 8–12 m (LWIR), in which the amount of IR radiation energy relies on the desired range of wavelength. The passive thermography consists of an IR camera, a control device, and a computer (processing unit) as shown in Fig. 10.3A.

It is generally a qualitative method with the primary aim of identifying discontinuities. This approach is widely applied as a standard quality control technique and has numerous applications, including condition monitoring, predictive maintenance, structural health monitoring, medical imaging, power station monitoring, building thermal efficiency, process monitoring, fire forest detection, road traffic monitoring, agriculture, and biological sciences [9]. Nevertheless, such an approach is sometimes restricted to NDT applications because there should be sufficient natural thermal contrast.
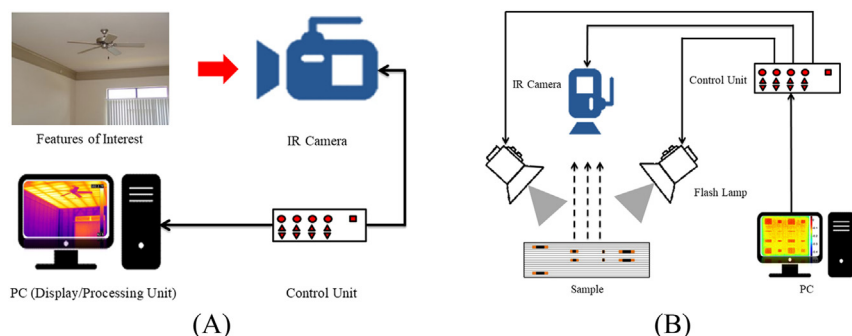
Figure 10.3 Experimental setup (A) passive, and (B) active thermography.

10.1.3.2 Active thermography

Active thermography integrates infrared imaging with an external energy source; that is, an external energy source is supplied to the subject being inspected, which was previously thermally balanced, and a temperature difference is generated to expose the details of interest. Active thermography, therefore, comprises an external energy source, a supply source, an IR camera, a control device, and a computer (processing unit), as shown in Fig. 10.3B. The experimental setup of active thermography is similar to passive thermography except that an external energy source is needed to produce a thermic inconsistency in the object or system. The heating or cooling energy can be generally supplied in pulsed or harmonically modulated form [10]. A wide range of energy origins can be employed for active thermography. Laser heating, optical flash lamps, halogen lamps, hot or cold air guns, electrical heating, ultrasonic excitation, eddy currents, microwaves, and other techniques are instances [11].

When a sample is heated or cooled, heat propagates by diffusion through the material, which has a direct impact on the surface temperature's temporal changes. Then, the thermal response of the investigated object, recorded by an IR camera, is evaluated to disclose the existence of imperfections. The assessment can take place in either transmission or reflection mode. In the transmission mode, the heating unit and the IR camera are on opposite sides of the object under examination, while in the reflection mode, the heating source and the IR camera are on the same side of the sample. Controlled testing conditions, including the quantity and type of stimulation, enable not only the detection of abnormalities but also the quantification of defects [12,13].

Active thermography provides different inspection methods as well as a variety of measuring techniques. Thus, the measurement procedure can be optimally adapted to different materials and parts with different structural properties. The inspection methods mainly differ in the type of excitation source used, the way thermal energy is applied, and the data/signal processing methods [14].

The primary classical practices are pulsed thermography (PT), step heating thermography (SHT), and lock-in thermography (LIT). In PT, short and high-power thermal energy is applied to the object's surface being inspected, and the thermal response of the stimulated surface is observed in a transient mode. PT is a fast and popular thermal imaging technique in non-destructive testing and evaluation (NDT&E). SHT is similar to PT, but in contrast, a longer pulse, from a few seconds to several minutes, is used for thermal stimulation, and the surface temperature of the stimulated object is monitored during both the heating and cooling phases. Whereas in LIT, the surface of the object being inspected is energized by a periodically modulated thermal wave, and the thermal response of the surface is observed in a steady-state condition [12,15].

Concerning the defect information, both filtering and efficient signal processing are of primary importance. By using the adapted image and signal processing strategies, it is possible to visualize discontinuities of different sizes inside structures or to inversely retrieve material thermal properties. Working with a reduced amount of thermal images speeds up the process, but inaccuracy increases, and these cons must be kept in mind. [16].

In NDT&E applications, active thermography can be used for the inspection of components/processes in various industries. Examples include investigation of interior structures such as lightweight honeycomb structures and recognition of deeper material deficiencies; detecting and characterizing defects such as metal corrosion, cracks, subsurface defects, coating wear, debonding, and impact damage; determining material properties such as thermophysical properties like diffusivity and thermal conductivity, adhesion strength, anisotropic material characterization, etc. [17].

10.1.4 Recent trends and developments

Since each NDT&E technique has its inherent limitations, integrating different methods is suggested for better inspection. In this regard, the fusion of IRT with other existing NDT&E techniques is rising. It will result in

better inspection capability, and more information can be acquired in a single test compared to the results of an individual technique.

The potential of combining thermography with shearography, an optical approach for identifying and characterizing subsurface defects in structures, has been investigated. Investigations have shown that by integrating two image-based NDT approaches, the suggested approach is suitable for defect detection [18].

Ultrasonics is the most mature and widely used method for NDT&E. The main advantage of ultrasound sensing is its outstanding capability to probe inside the object, with the disadvantage of being contacted and a low-productive technique. Hence, the integrated use of IRT with ultrasonic sensing may be advantageous to detect both shallow and deep defects, saving time during the inspection of large surfaces [19]. In this integrated approach, heating of the material under inspection can be accomplished via the application of sonic or ultrasonic energy using a device such as an ultrasonic welding horn known as vibrothermography, thermosonics, or sonic infrared.

Eddy current can be combined with IRT, in which the object under inspection is heated by an inductively generated current flow, which is known as induction thermography. This integrated technique uses induced eddy currents to heat the material being tested, and defect detection is based on the changes in the induced eddy current flow revealed by the thermal distribution captured by the infrared camera.

In some cases, even more than two NDT methods can be fused. For example, eddy current, IRT, and laser scanning were used in combination to inspect aeronautical structures such as honeycomb sandwich panels that have been damaged by low-velocity impacts [20].

10.2 Data analysis

Raw thermal data are generally not suitable for the quantitative evaluation of defects. Several preprocessing and processing techniques to enhance the detection capability and evaluation metrics to characterize the performance of the processing techniques have been developed.

10.2.1 Conventional techniques

Some preprocessing techniques such as pseudo-colorization, histogram equalization, image filters—a median filter and a gaussian low filter—segmentation, image fusion, image building, image subtraction, etc. are integrated features

in the typical R&D software in infrared cameras. These preprocessing techniques mainly help to reduce the effects of nonuniform surface emissivity, temporal noise, spatial image noise, and outliners caused by dead pixels. Besides these, several studies demonstrate the development of processing techniques and their effectiveness in detecting and assessing defects. Table 10.1 depicts a simple classification of thermal data processing techniques based on image

Table 10.1 Classification of thermal data processing based on image processing groups [21,22].

Groups	Techniques	Remarks
Thermal contrast	Absolute contrast running contrast normalized contrast standard contrast differential absolute contrast	1-D solution of Fourier's diffusion equation for pulsed thermography and enables to model the time evolution profiles of the sample surface temperature. Enhanced the defect contrast for pulsed thermography data.
Transforms	Harmonic approximation (four point method)	Fast method and only valid for sinusoidal stimulation. Enhanced the defect detectability for modulated thermography.
	Fast Fourier transform Wavelet transform	Enhanced the defect detectability for both pulsed and modulated thermography. Also used in the passive thermography approach.
	Pulsed phase thermography	Enhanced the defect detectability for pulsed thermography data.
	Principle component analysis	Usually used to enhance the defect detectability for pulsed thermography data. But can also be used for modulated thermography, though efficiency needs to be evaluated. Also used in the passive thermography approach.
Statistical	Signal reconstruction, derivatives, skewness, kurtosis	Enhanced the defect detectability for Dirac and square pulsed thermography.

processing groups, that is, techniques based on thermal contrast, techniques based on transforms, and techniques using statistical methods.

Although there are several data processing techniques, computation of the amplitude image and phase image using the Fourier transform is the most popular technique in active thermography, specifically for both pulsed and modulated thermography. The Fourier transform is used to pass from time to the frequency domain in thermal images. The Discrete Fourier Transform (DFT) is implemented for each pixel of the thermographic data set and can be expressed by Eq. (10.5) [17]:

$$F_n = \Delta t \sum_{k=0}^{N-1} T(k\Delta t)\exp^{\frac{j2\pi nk}{N}} = Re_n + Im_n \qquad (10.5)$$

where Δt is the sampling interval, j is the imaginary number, n is the frequency increment ($n = 0, 1, \dots N$), and R_e and I_m are real and imaginary parts of the transform, respectively. To simplify, the Fast Fourier Transform is used instead of the DFT and is available in the standard software package. With the transformation of data to the frequency domain, the amplitude (A_n) and phase angle (φ_n) in different frequencies are computed using Eqs. (10.6) and (10.7), respectively [17]:

$$A_n = \sqrt{R_e^2 + I_m^2} \qquad (10.6)$$

$$\varnothing_n = \tan^{-1}\left(\frac{Im_n}{Re_n}\right) \qquad (10.7)$$

The phase image is not directly linked to local disturbances, for example, nonuniform heating and emissivity; in fact, it is related to the depth attained by the thermal wave. Hence, phase images are used in the identification of defects.

Literature shows different types of evaluation criteria to characterize the performance of the processing techniques. The signal-to-noise ratio, also known as the contrast to noise ratio (CNR), is an evaluation metric to determine and qualify the advantages and limitations of each processing technique. Also, the CNR metric is used to differentiate the two regions of interest (ROI). The quantification of a defect is based on the information of two areas: the defective area and the reference or sound area. Contrast is the absolute difference between the defective area information and the sound area information. Noise is the standard deviation of the

noise area information. Information may be in temperature, amplitude, or phase angle, depending on the type of image. For this purpose, two ROIs, one for each defective area and one adjacent to the defective area (i.e., sound area), are selected. ROI in the defective area will be considered as "signal" (DROI), and ROI in the sound area will be considered as "noise" (SROI). The CNR metric for a defect can be calculated by using Eq. (10.8) [22]:

$$\text{CNR} = 20\log_{10}\left(\frac{|\text{DROI}_{\text{mean}} - \text{SROI}_{\text{mean}}|}{\sigma}\right) \qquad (10.8)$$

where $\text{DROI}_{\text{mean}}$ is the arithmetic mean of the defective area; $\text{SROI}_{\text{mean}}$ is the arithmetic mean of the sound area; and σ is the standard deviation of the defective area.

10.2.2 Advanced techniques

The analysis of temperature evolutions in both defective and sound regions is central to IRT data processing. In both passive and active thermography, the data recorded with infrared cameras can be considered in three different forms in order to be processed: a 1-D model which is independent of spatial information and where input is a vector of temperature history in terms of time for a pixel; a 2-D model which is independent of temporal information and where input is thermal images; and a 3-D model with the input of thermal images (video) series combining the 1-D and 2-D models.

Artificial intelligence's rapid advancement, particularly Machine Learning (ML) and Deep Learning (DL), makes IRT increasingly automated and intelligent, broadening its scope of applications significantly [23]. For instance, Recurrent Neural Networks (RNN) and 1D Convolutional Neural Networks (CNN), 2D CNN, and 3D CNN are the popular DL methods based on the format of the input corresponding to 1D, 2D, and 3D models, respectively. On the other hand, compared to visible images, the quantity of labeled thermal images is significantly lower; thus, various challenges arise. Utilizing labeled VL data to minimize the quantity of data necessary for IRT algorithms in DL is a fascinating topic. Transfer learning [24] is an ML method that focuses on storing and transferring information obtained while addressing one problem to a different but related task. Domain adaptation [25] is a particularly effective approach to transfer learning when the data is diverse but the tasks are the

same. Common VL tasks, like object detection, offer passive IRT with a wide range of expertise and data [23]. The DL algorithms that have recently been used to analyze IRT data are explained in the following within the two categories of passive and active IRT.

10.2.2.1 Deep learning in passive infrared thermography

In passive IRT, the use of DL models such as RNN, CNN, Generative Adversarial Network (GAN), Auto-encoder (AE), and Restricted Boltzmann Machine is often more prevalent than in active IRT. Since IR cameras have an inferior resolution to visual cameras, resulting in a poor-quality image and restricted use of passive IRT, several researchers have evaluated CNN [26] and GAN [27] to boost the resolution of IR projections. To increase the resolution of thermal images, single-frame superresolution technology might be used. For instance, the enhancement of the quality of infrared images for object detection was studied in [28]. To enhance target signature quality and maximize the baseline resolution of inputs, a method according to Super-Resolution CNN (SRCNN) and image bias correction has been suggested. The key goal is to improve the amount of usable information on the item to be identified, even if the quantity of target pixels is insufficient. The method improved target resolution substantially in experiments, allowing automated detection systems to recognize objects more efficiently. Instead of just merely improving the resolution of thermal data, some researchers are attempting to exploit the synergy of visual and thermal images to combine their information for super-resolution. For example, a DL method according to GAN was established, improving the resolution of thermal images by integrating VL and IRT data [29]. An approach combining a GAN with a residual network has been suggested to enhance the visualization of the fusion of thermal and visible images [27]. Experiments show that the suggested technique finally produces suitable results, outperforming nine representative thermal and visible image fusion methods in terms of visual resolution and objective assessment.

10.2.2.2 Deep learning in active infrared thermography

Although the use of DL in active IRT is currently lower than in passive IRT, its advancement and growing use are expected in this regard. DL in active thermography NDT&E can be categorized into three subdivisions depending on the format of the input data, as earlier mentioned above since active IRT generally creates thermal video.

10.2.2.2.1 1-D model

A Long Short-Term Memory Recurrent Neural Network (LSTM-RNN) model based on an array of temperature series [30] has been used to automatically classify prevalent defects in honeycomb materials, such as adhesive pooling, debonding, and liquid ingress. The proposed LSTM-based algorithm has a sensitivity of more than 90% in identifying water and hydraulic oil ingress and more than 70% in classifying adhesive pooling and debonding.

In LIT, a 1D CNN model is used to evaluate the thermal sequence of Carbon Fiber Reinforced Polymer (CFRP) specimens [31]. A new two-stream CNN structure is utilized to draw features from a pair of 1D thermal signal series to accurately classify faulty and healthy areas. In comparison to PCA and the Fourier transform, the results show that the 1D CNN improves resolution.

10.2.2.2.2 2-D model

For surface crack detection, 2D CNN has been employed [32]. A DL-based autonomous concrete fracture detection approach integrating vision and IRT data has been provided. By spatially inspecting via unmanned vehicles equipped with a hybrid imaging technology that includes IR and vision cameras as well as a continuous–wave line laser, concrete–made infrastructure on a large scale (like bridges and dams) can be efficiently assessed. To accomplish automatic crack detection and visualization, the reconstructed images have been categorized into multiple patches, and each patch has been categorized using a pretrained GoogLeNet using a transfer learning approach.

10.2.2.2.3 3-D model

Active thermography's growing development is the 3D model, which integrates temporal and spatial data. Nonetheless, since 3D input has the complexity to tackle, several approaches have been developed that can help, such as:

• **Reducing temporal data:** Since it is troublous to utilize DL to analyze temporal and spatial data at the same time, some researchers suggest compressing temporal data with a non–DL approach first, then processing spatial data with a DL one [23]. For instance, to provide accurate crack identification and localization, an end–to–end pattern deep region learning architecture has been suggested [33]. The temporal information was extracted from the thermal video using PCA and

compressed into a single frame (matrix) with a more substantial defect feature, while Faster–RCNN was used to detect faults from the matrix.

- **Dealing with temporal and spatial data independently:** This category, for instance, can be found in Ref. [34]. A technique integrating YOLO (Yolonet—you only look once) and a fully connected network (FCN) has been presented, according to the hypothesis that the spatial and temporal data in thermal sequences are unrelated. FCN forecasts the depth of defects, whereas YOLO evaluates if there are any. The approach may be considered as a fusion of a 1D feedforward network and a 2D YOLO model.
- **Designing a fused temporal–spatial network:** To analyze merged temporal and spatial inputs, a hybrid spatial-temporal DL framework for automated thermography has been developed [35], notwithstanding the difficulty. An LSTM (with 3 layers) loop has been used to collect the material characteristics that reflect the character of thermal differences between the defective and the healthy point, and Visual Geometry Group-Unet (VGG-Unet) has been employed for identifying the faulty area out of the standard.

10.3 Modeling and simulation

Modeling is the process of representing an actual system in a mathematical form with its properties, while simulation is an experiment based on a developed model implemented into a computer program to study the performance of a system. Modeling and simulation provide insight into how systems can behave early in their lifecycle without the risk and expense of building the system and transporting it to the environment concerned. Thus, modeling and simulation enable rapid and cost-effective analysis of complex systems, thereby reducing development time and costs. Over the past few decades, modeling and simulation have been booming with their applications in engineering and computer sciences, military and defense, aerospace and transportation, education, health care and drugs, recreation and entertainment, architecture and construction, climate and environment, finance and economics, etc. [36].

Modeling and simulation consist of four main steps: conceptual modeling, mathematical modeling, numerical modeling, and computational modeling. Conceptual modeling puts the problem in the context of its physical phenomenology and allows the information needed for a

good system design to be structured and ordered. Mathematical modeling systematically analyzes phases and components together with the constitutive laws to derive the balance equations and the initial and boundary conditions. Numerical modeling choose a convenient way of discretizing equations based on the shape of the balance equations and the mathematical restrictions of the problem. Computational modeling chose a suitable computational platform with a computational language and software for writing the numerical model once the numerical model has been finalized [37].

Modeling and simulation studies typically fall into four types of applications: proof-of-concept, modification, comparison, and optimization. Proof-of-concept studies are executed in the predesign phase of a future system, support the determination of the viability of concepts, and provide information concerning the expected system performance. Modification studies are conducted on existing systems to allow inferences regarding system performance under proposed operating conditions and to allow parameter settings to be tuned for desired system prediction accuracy. Comparison studies involve competing systems. Finally, the determination of the best system operating conditions is based on optimization studies [38].

Modeling and simulation are used in many steps of the NDT&E process, specifically for the development and verification of new inspection methods. Many researchers from around the globe have used modeling and simulation to stimulate the propagation of the thermal wave in materials for IRT inspection. Shrestha et al. [13] developed a transient finite element model using commercial software, "ANSYS 15," and simulated PT and LIT to evaluate the coating thickness, stimulated by a flow of heat, allowing experimental parameters to be tailored without the need for extensive, time-consuming, and potentially expensive preliminary experiments. The same authors [39] used modeling and simulation to develop a PT inspection process to detect artificial flat-bottomed hole defects in aluminum structures using "ANSYS 15." Shrestha et al. [40] also developed a transient finite difference model and simulated the LIT inspection process to detect inclusions in glass fiber–reinforced plastic composite structures using the software "ThermoCalc–3D." Shrestha et al. [41] used a transient finite element model and stimulated a flow of heat to simulate PT for the evaluation of ancient marquetry samples using "ANSYS 19." Tighe et al. [42] created the finite element model of PT and PPT to detect the kissing defects in adhesive bonds.

To obtain the results shown in Fig. 10.4, the authors used commercial software "ANSYS 15" and modeled a square-shaped coating sample of size 180×180 mm with a nickel–based superalloy substrate of 4 mm, a bond coat of MCrAIY of 0.1 mm, and a top coat of zirconia varying from 0.1 to 0.6 mm. In this work, the authors used a tetrahedral fine mesh. Also, physical preference was taken into account as mechanical with a relevance equal to 100. Finally, the relative center worked in fine mode, while both proximity and curvature were used in the advanced size function. The final mesh had 162,000 elements, while the nodes were 854,685 in total. In PT configuration, an energy of 9 kJ was delivered via a single square pulse of heating lasting 10 ms. The frame rate was set at 0.01 seconds and the analysis lasted 5 seconds. In the LIT configuration, a 2 kW power was applied as a heat stimulus. The time step was retrieved by the modulation frequency, and the period of analysis was defined as $\frac{2}{100f}$. Here, f is the modulation frequency. Several modulation frequencies ranging from 1 Hz down to 0.01 Hz were used in the simulation. On this basis, the authors concluded that the simulation model helps a better understanding of PT and LIT modalities by both optimizing the experimental configuration and limiting the number of physical tests. It is possible to underline the fact that both thermographic techniques are useful for an accurate and fast determination of coating thickness.
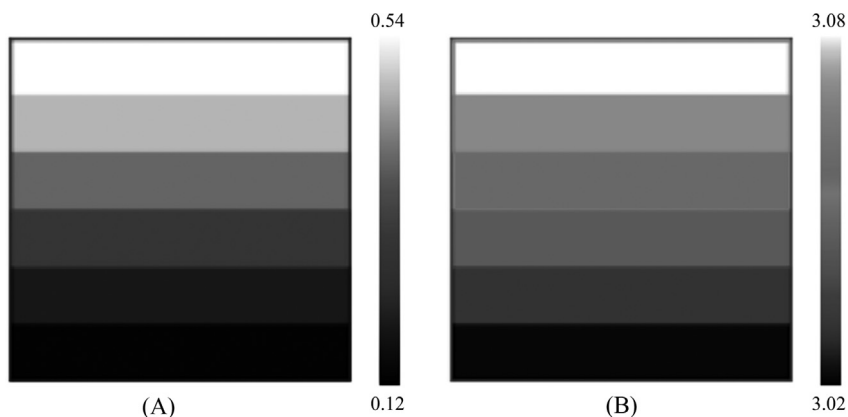

Figure 10.4 Phase angle data with respect to variation in coating thickness, (A) Phase image obtained after the processing of PT data using Fourier transform and (B) Phase image obtained after the processing of LIT data at the modulation frequency of 0.2 Hz [13].

10.4 Relevant standard

Recently, structural health monitoring of the components, specifically using IRT, has expanded rapidly in various areas. The effectiveness of IRT inspection depends on the proper use of the systems and equipment. The International Organization for Standardization (ISO) provides terms, basic principles, equipment, and test procedures, as well as matters related to international certification of thermal imaging. Currently, the ISO technical committee, ISO / TC 135/SC 8—Thermographic testing in NDT, is in the process of standardizing "Electrical Equipment Testing" as ISO 5750 in WG 4 and "Testing Method for Integrated Performance" as ISO 18251-2 in WG 3 [43]. Table 10.2 presents some of the ISO standards developed regarding IRT testing.

In addition, the American Society for Non-destructive Testing and American Society for Testing and Materials in the United States, the Deutsches Institut für Normung in Germany, the British Standards Institution in the United Kingdom, and the Japanese Society for Non-Destructive Inspection (JSNDI) in Japan standardize IRT tests, use standards for every measuring and diagnostic case, and also issue certificates.

10.5 Case study

The high quality of materials and structures is of paramount importance in different areas of human activity. Steel is used around the world because of its good chemical–physical and mechanical qualities.

It should be highlighted that multiple preparations and cautions should be taken into consideration in order to effectively perform IRT inspection and avoid further errors throughout the assessment of metallic samples. Since the reflectivity of the object's surface, particularly for metal objects, is one of the key obstacles in IRT, an opaque (color) cover can be sprayed on the surface. This solution, however, cannot be used on any item, such as a painting or artwork [52]. Another situation is when IRT performance is being evaluated. Several mechanical and thermal characteristics should be considered and appropriately modeled in order to simulate a true representation of a realistic defect in the lab and research. The most important characteristic is the relative thermal conductivity of the primary material to the imperfection. For example, Teflon, which is commonly used to simulate defects such as delamination and detachments in composite structures including CFRP and GFRP, should not be used because of

Table 10.2 ISO standards related to thermographic testing.

Group	Standard identification	Remarks
ISO	ISO 10878: 2013—Non-destructive testing—Infrared thermography—Vocabulary [44]	Defines terms used in IRT for NDT and forms a common basis for standard general use.
	ISO 10880: 2017—Non-destructive testing—Infrared thermographic testing—General principles [45]	Provides general principles for IRT testing in the field of industrial NDT.
	ISO 18251−1: 2017—Non-destructive testing—Infrared thermography—Part 1: Characteristics of system and equipment [46]	Describes the main components and their characteristics, constituting an infrared imaging system and related equipment used in NDT. It also aims to assist the user in the selection of an appropriate system for a particular measurement task.
	ISO 22290: 2020—Non-destructive testing—Infrared thermographic testing—General principles for thermoelastic stress measuring method [47]	Provides general principles for thermoelastic stress measuring method of IRT testing in the field of industrial NDT.
	ISO 18434−1: 2008—Condition monitoring and diagnostics of machines—Thermography—Part 1: General procedures [48]	Introduces the application of IRT to machinery condition monitoring and diagnostics, where "machinery" includes machine auxiliaries such as valves, fluid and electrically powered machines, and machinery related heat exchanger equipment.
	ISO 18434−2: 2019—Condition monitoring and diagnostics of machine systems—Thermography—Part 2: Image Interpretation and diagnostics [49]	Provides specific guidance on the interpretation of infrared thermograms as part of a program for condition monitoring and diagnostics of machine systems.
	ISO 18436−7: 2014—Condition monitoring and diagnostics of machines—Requirements for qualification and assessment of personnel—Part 7: Thermography [50]	Specifies requirements for qualification and assessment of personnel who perform machinery condition monitoring and diagnostics using IRT.
	ISO 9712:2012—Non-destructive testing—Qualification and certification of NDT personnel [51]	Specifies requirements for principles for the qualification and certification of personnel who perform industrial NDT including IRT.

its similar thermal conductivity coefficient to the polymer matrix of CFRP and GFRP [53]. In other words, when it comes to assessing IRT, Teflon is not really an acceptable simulator for defects in polymeric composite materials.

A steel sample, shown in Fig. 10.5, was inspected by PT and LIT. The sample consists of flat–bottomed hole defects to simulate subsurface defects. The authors used on the front side a KRYLON flat paint with an emissivity of 0.95, with the aim of providing a uniform value of emissivity on the entire inspected surface.
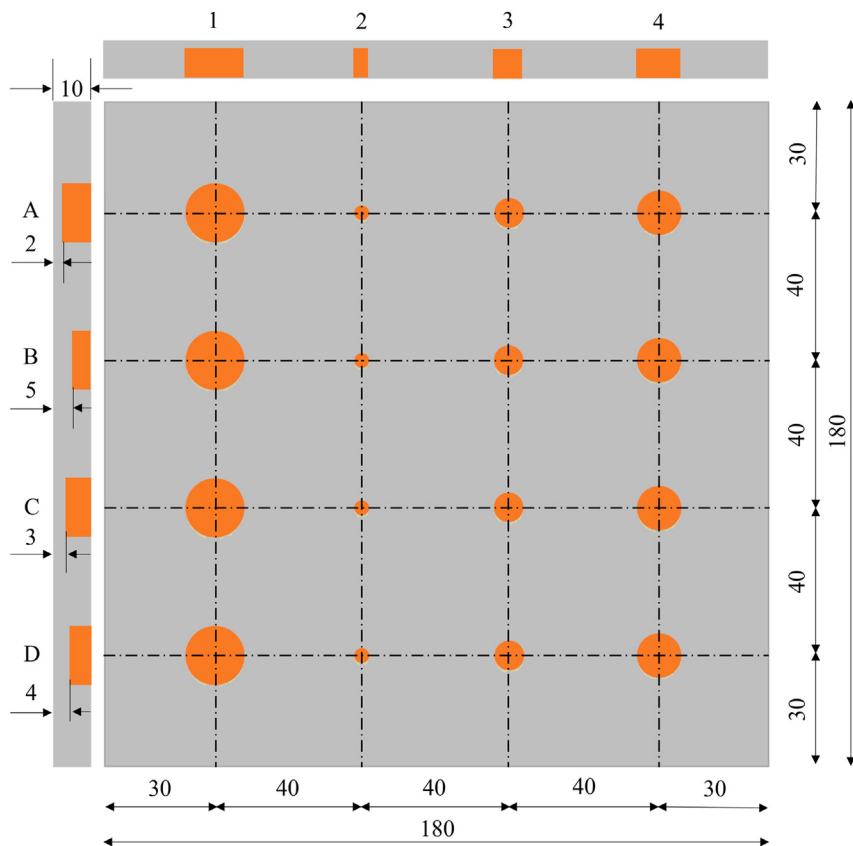

Figure 10.5 Schematic illustration of stainless-steel sample along with the geometry and location of artificial flat-bottomed holes representing subsurface defects of different sizes at varying depth levels [12].

10.5.1 Lock-in thermography

The experiment was conducted with a lock–in system in reflection mode. The lock–in system consisted of an IR camera (SC 645, FLIR Systems, Danderyd, Sweden) with a 640×480 pixel resolution, a spectral range of $7.5-13$ µm, thermal sensitivity (NETD) <50 mk, accuracy $\pm 2°C$, and a frame rate of 50 Hz; a heat source (two halogen lamps (OSRAM, Medium Flood, China) of 1 kW each); a programmable function generator (Agilent 33210A, Malaysia); a lock–in module (Answer Tech, Republic of Korea); and a personal computer (MSI GE620DX).

Fig. 10.6 shows the phase images acquired at modulation frequencies of 0.1, 0.05, 0.02, and 0.01 Hz. The phase image is considered superior to the amplitude image because it is independent of local disturbances such as nonuniform heating and emissivity and is primarily influenced by the
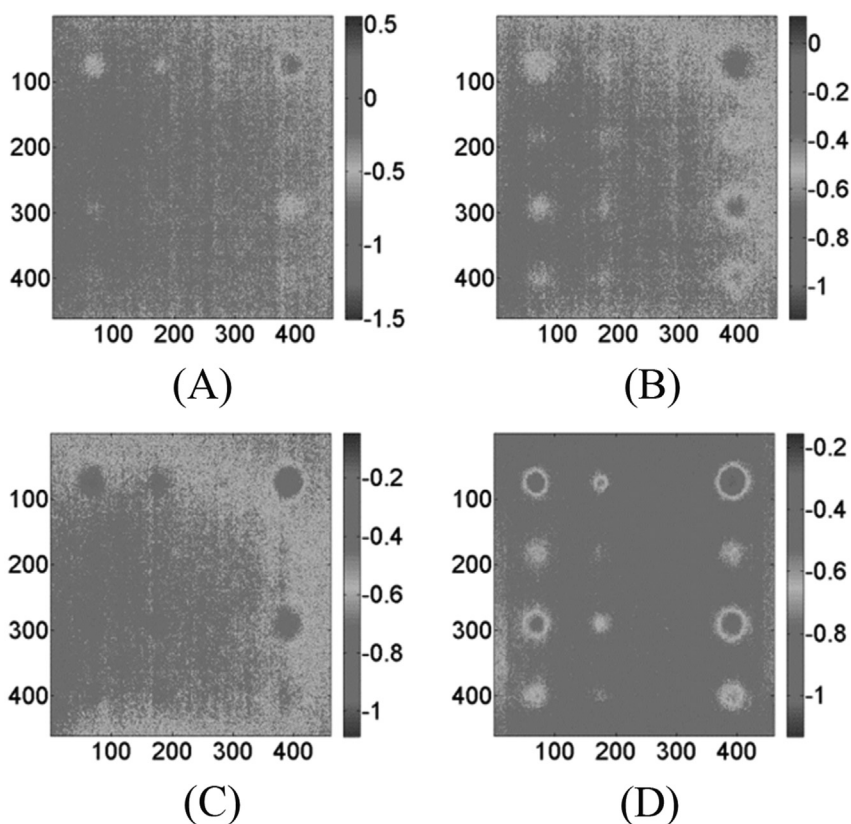

Figure 10.6 Phase images using LIT at modulation frequencies, (A) 0.1 Hz, (B) 0.05 Hz, (C) 0.02 Hz, and (D) 0.01 Hz.

depth attained by the thermal wave. It is possible to see that no defects were detected at the highest frequencies of 0.1 Hz. While the frequency is lowered to 0.05 Hz, the contrast begins to improve, and when it decreases to 0.01 Hz, the subsurface defects in phase images become clearly visible. It can also be seen that there is a phase contrast between the defective areas and the sound areas. Hence, the correct modulation frequency range has to be selected for the material to detect defects.

10.5.2 Pulsed thermography

The experimental setup is based on a short and high-power heating source lamp (Universal BALCAR, Rungis, Paris, France) of power 6400 W-s with the system controller (BALCAR Light System, Nexus A 6400, France), an infrared camera (FLIR Systems, Danderyd, Sweden) with a spectral range of 7.5−13 μm, thermal sensitivity (NETD) <50 mk, accuracy ±2°C, a 640 × 480 focal plane array detector with a frame rate of 50 Hz, and a personal computer (MSI GE620DX). The front side of the sample surface was subjected to a heat pulse with a duration of ∼10 ms. In addition, 5 seconds was the duration of the registration of the thermal response. The results obtained through some of the conventional and advanced techniques are discussed here.

10.5.2.1 Thermal signal reconstruction

The result of Thermal Signal Reconstruction (TSR) is illustrated in Fig. 10.7A. Also, in order to convert the obtained image to the binary one aimed at a better comparison, a thresholding method based on local intensity is utilized,
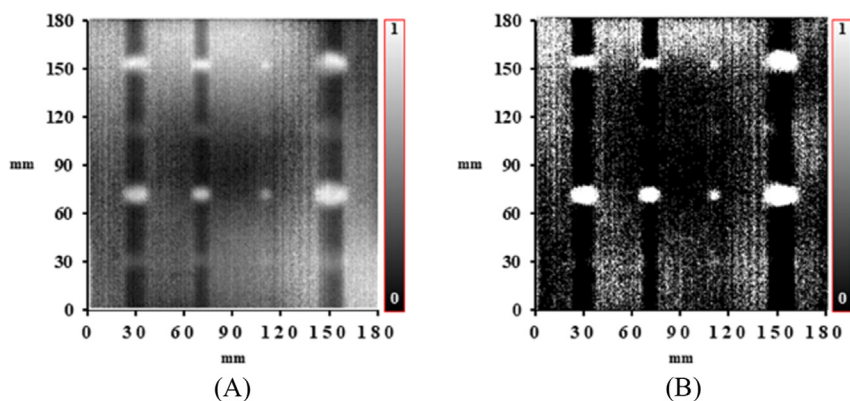

(A)   (B)

Figure 10.7 Results of TSR algorithm with the maximum kurtosis value among frames: (A) Gray image and (B) Binary image. Axes units are mm.

which determines a different threshold at each pixel by the Gaussian weighted mean in the neighborhood. Hereinafter, the results are converted to binary images using this local thresholding. The binary result of TSR is illustrated in Fig. 10.7B. The frame has been selected at the moment with the maximum kurtosis value for that frame having an acceptable contrast. The TSR method was able to detect shallower defects with a depth of 2 and 3 mm but not deeper defects with a depth of 5 and 4 mm.

10.5.2.2 Pulse phase thermography

The amplitude and phase of PPT, as well as their binary results, are shown in Fig. 10.8. The images have been selected with the maximum kurtosis value for that frame. Nevertheless, since the result of the amplitude of PPT at the maximum kurtosis moment is not proper, another (last) frame is also displayed in Fig. 10.8, in which all defects can be somehow traced. Nevertheless, the fault size cannot be precisely and simply approximated.

10.5.2.3 Principle component thermography

The first five principle components (PCs) obtained by PCT and their binary images can be seen in Fig. 10.9. The influence of nonuniform
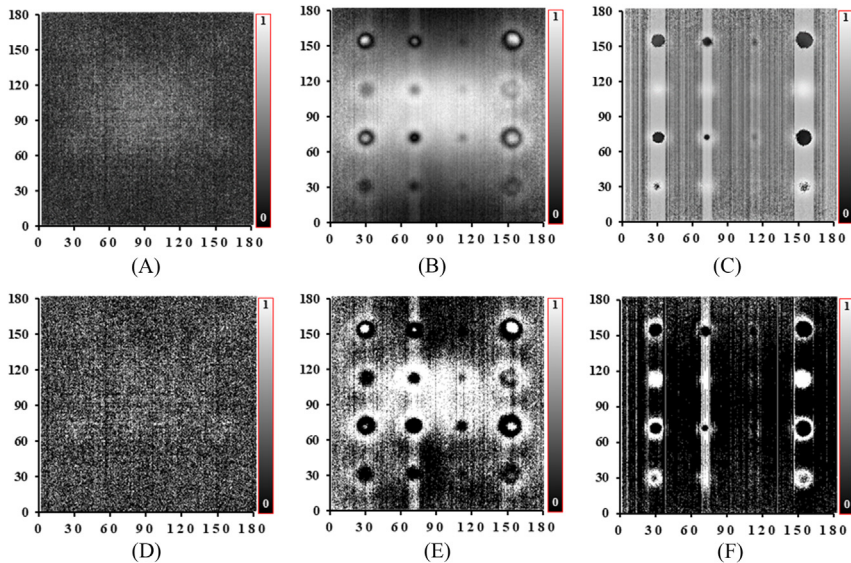

Figure 10.8 Results of PPT algorithm, (A) Gray PPT amp (Max Kurtosis) image, (B) Gray PPT amp (last frame) image, (C) Gray PPT Phase (Max Kurtosis) image, (D) Binary Gray PPT amp (Max Kurtosis) image, (E) Binary PPT amp (last frame) image, and (F) Binary Gray PPT Phase (Max Kurtosis) image. Axes units are mm.
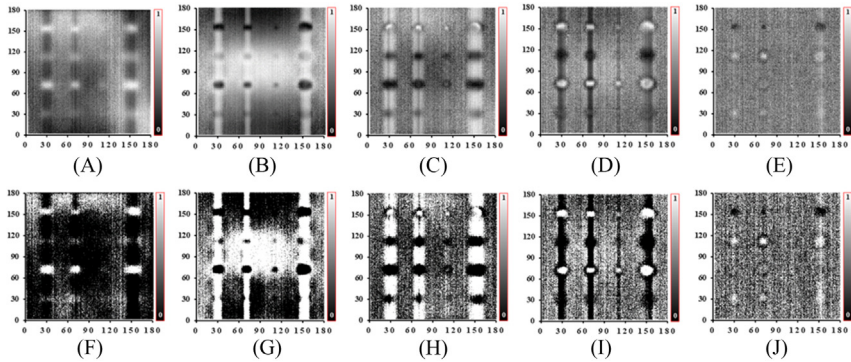
Figure 10.9 Results of PCT algorithm, (A) Gray image 1st PC, (B) Gray image 2nd PC, (C) Gray image 3rd PC, (D) Gray image 4th PC, (E) Gray image 5th PC, (F) Binary image 1st PC (G) Binary image 2nd PC, (H) Binary image 3rd PC, (I) Binary image 4th PC, and (J) Binary image 5th PC. Axes units are mm.

heating distribution may be noticed in the first and second PCs, and as a result, the third and fourth PCs can better confirm the existence of all defects. In addition, as shown in Fig. 10.10, some of the PCs can be combined in order to synergy of the performance because the resolutions of different defects in different PCs are varied, and it cannot be confirmed that one PC exists that has the highest resolution for all defects with different depths compared to other PCs.

10.5.2.4 Thermal signal area
Thermal Signal Area (TSA) combines each pixel's thermal response across a user-defined timespan [54,55]. The results of TSA for a time range from the 10th frame to the 100th frame are shown in Fig. 10.11. Although not all defects can be detected, particularly the deeper and smaller ones, this method is fast and simple to use. It should be noted that the TSA is more suitable for step and long pulse heating thermography methods. In addition, the TSA-inspired Adaptive Spectral Band Integration (ASBI) approach [56], considering the frequency domain instead of time domain, can be utilized to better analyze the thermograms.

10.5.2.5 Artificial neural network
In this section, a Pattern Recognition Neural Network (PRNN) in three simple architectures is used to classify the pixels. In fact, the thermal variation of each pixel over time is considered a timeseries signal, and as a result, a thermal video can be considered a multitimeseries. Then, a
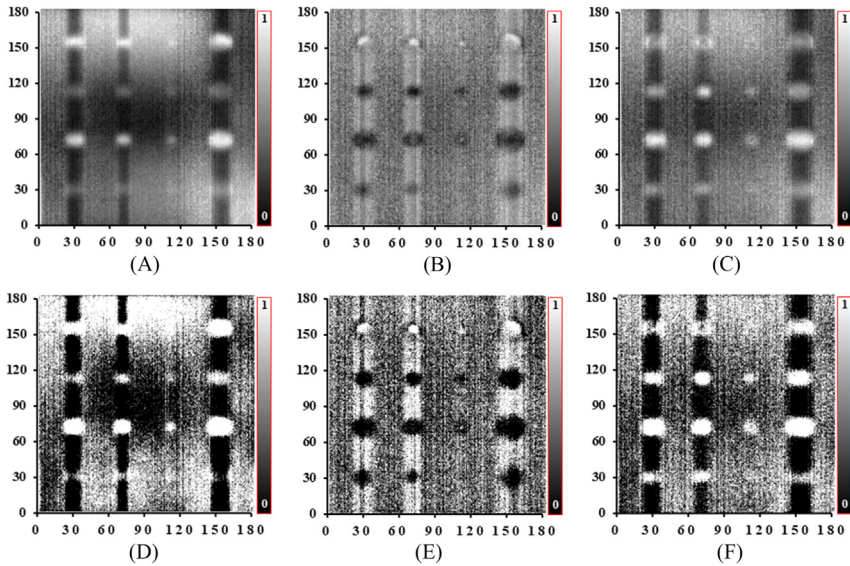
Figure 10.10 Results of PCT algorithm, (A) Gray image superposition of PC1 and PC2, (B) superposition of PC3 and PC5, (C) Gray image superposition of PC1, PC2, PC3, and PC5, (D) Binary image superposition of PC1 and PC2, (E) Binary image superposition of PC3 and PC5, and (F) Binary images superposition of PC1, PC2, PC3, and PC5. Axes units are mm.
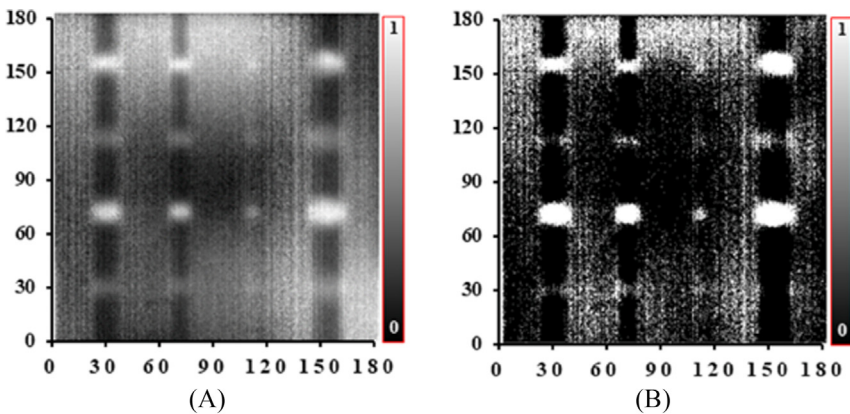

Figure 10.11 Results of TSA algorithm, (A) Gray image, and (B) Binary image. Axes units are mm.

PRNN can be used to classify these timeseries related to different pixels to determine which pixels are sound (intact area of the inspected sample) and which ones are defective (defective area of the inspected sample). Here, the problem is considered as a supervised NN for classification with

two classes: sound (0) and defective (1). Three architectures for PRNN are:

- 1st architecture: one hidden layer with 10 neurons.
- 2nd architecture: one hidden layer with 20 neurons.
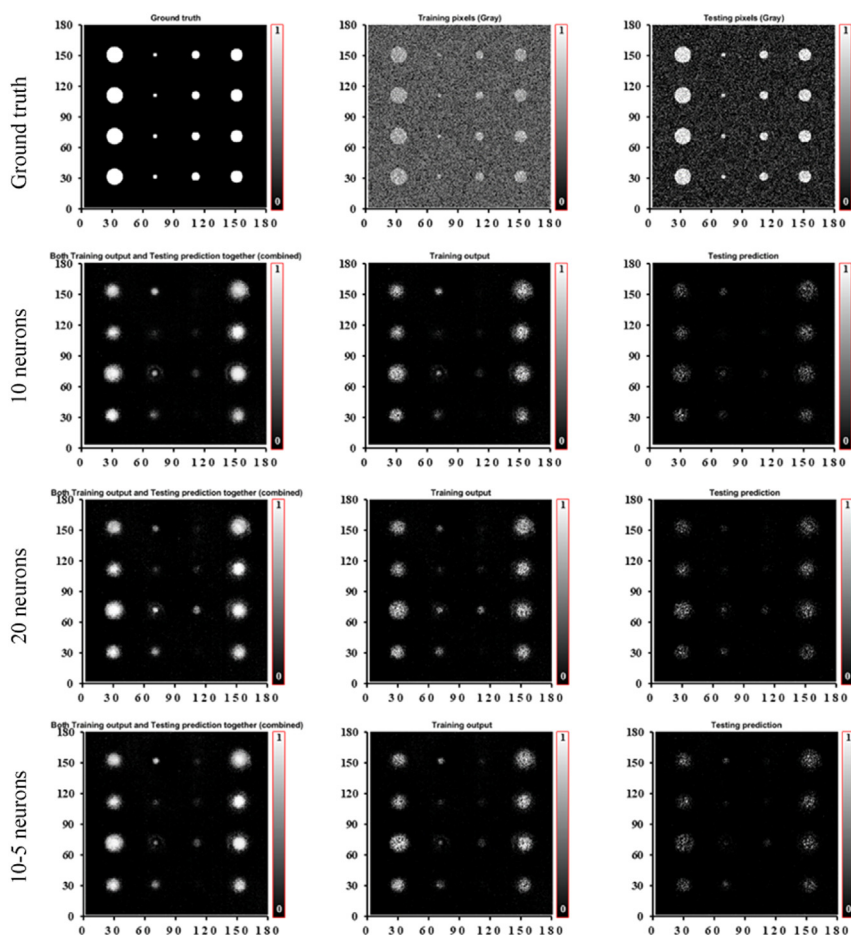- 3rd architecture: two hidden layers with 10 and 5 neurons, respectively.

Figure 10.12 Results of PRNN on thermograms (raw data). First row: Ground truth image (*left side*), ground truth image including training (*gray*) pixels (*middle*), and ground truth image including testing (*gray*) pixels (*right side*); second row: the results of architecture 1; third row: the results of architecture 3; fourth row: the results of architecture 3. Axes units are mm.

   Scaled conjugate gradient backpropagation is used to train the networks. First, a ground truth image is made in which 1 (white color) is a defective pixel and 0 (black color) is a sound pixel. Next, the dataset containing multitimeseries signals is randomly divided into training and testing datasets by a ratio of 7:3. It should be noted that the training dataset itself is also divided into (pure) training and validation datasets by a ratio of 4:1 in order to perform validation checks during training. Thus, the ratio of the training to the total dataset is 56%. Since only one specimen is evaluated in the present work, this type of division for the training and testing
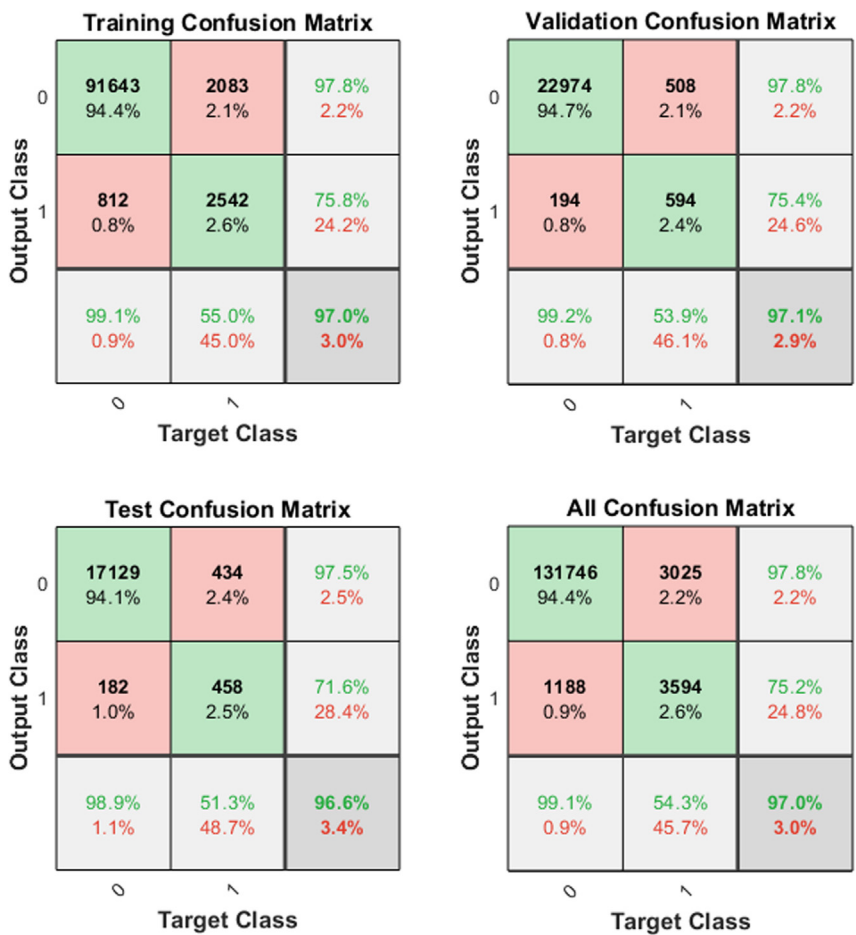

Figure 10.13 Confusion matrix of PRNN for the first architecture with 10 neurons on thermograms.

dataset is applied. Otherwise, if more specimens were available, the results would be improved. The ground truth image as well as the training and testing pixels highlighted in gray on the ground truth image can be seen in Fig. 10.12 (first row). Despite the lack of a sufficient training dataset for utilizing a supervised NN and the model's simplicity, the majority of the faults may be spotted.

The neural networks' performances are calculated based on cross-entropy. The performances (MAE) for architectures 1, 2, and 3 on the raw thermal data are 0.0884, 0.0832, and 0.085, respectively. Also, the
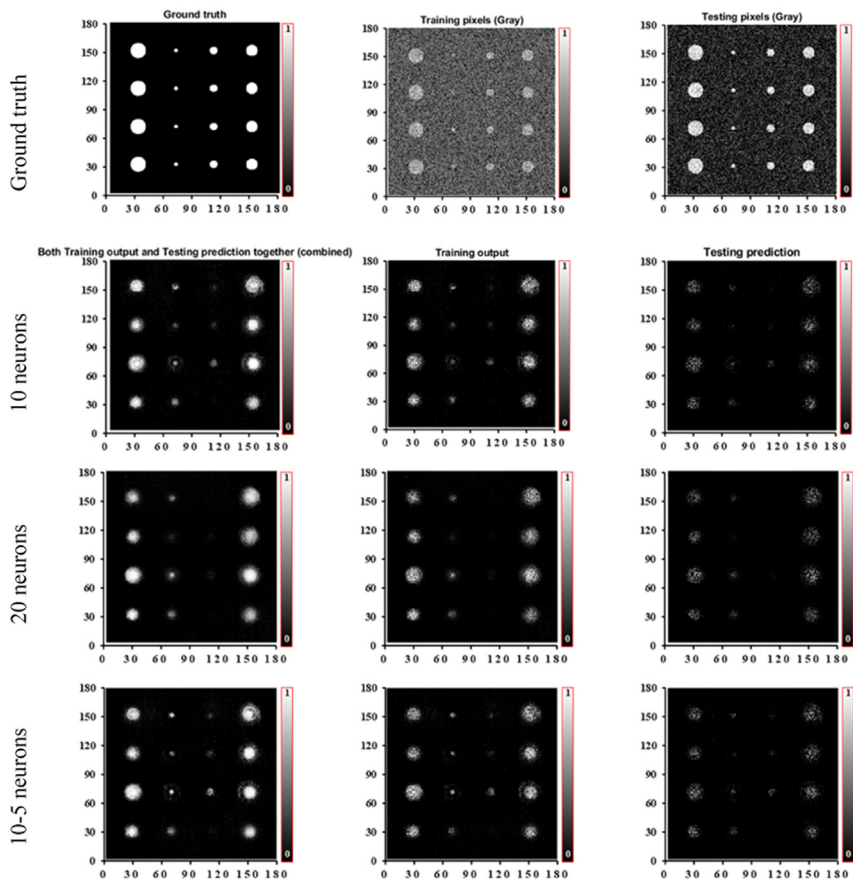

Figure 10.14 Results of PRNN on processed data (TSR). First row: Ground truth image (left side), ground truth image including training (*gray*) pixels (*middle*), and ground truth image including testing (*gray*) pixels (right side); second row: the results of architecture 1; third row: the results of architecture 3; forth row: the results of architecture 3. Axes units are mm.

confusion matrices for the first architecture are shown in Fig. 10.13. The results confirm that artificial neural networks (ANN) have strong efficiency in detecting defects in thermal videos.

In another scenario, the NN models can also be applied to the processed data by using some common algorithm. For example, the results of the three aforementioned PRNN architectures applied to the de-noised data by the TSR method can be seen in Fig. 10.14. The performance (MAE) for architectures 1, 2, and 3 on the TSR video are 0.0891, 0.0945, and 0.0793, respectively. The results are superior with the deeper NN, which has 10 and 5 neurons in the first and second layers, respectively.

The results are acceptable, and the defects can be detected, even though the PRNN architecture was not optimized and is simplistic. With a deeper neural network, the outcomes could be much improved. The application of the DNN in IRT has dramatically increased recently [57], and advanced, mature DNN frameworks and architectures were introduced for thermography [35,58].

10.6 Conclusions

The chapter has been organized into six sections, comprising this one. The logic follows a pyramid scheme, that is, the so-called top-down approach. Initially, an overall view of the IRT technique has been given; therefore, the authors have deepened the main concepts of data analysis; subsequently, experience in thermal modeling and simulation has been provided to the readers, who anticipated the state-of-the-art in relevant standards; and finally, a series of case studies has taken stock of the technique itself.

The chapter is actualized to 2022 since it provides the recent advances of numerical modeling as a facilitator to understanding experimental analyses. The latter rests on a case study dissected through the implementation of well-known and advanced algorithms for image processing, up to the core, that is, an ANN example applied to a stainless-steel sample having flat-bottomed holes representing subsurface defects of different sizes at varying depth levels. The results obtained can be considered of great interest and leave the doors open for future perspectives, such as the fusion of images with other NDT techniques.

References

[1] J.F.W. Herschel, I. on the chemical action of the rays of the solar spectrum on preparations of silver and other substances, both metallic and non-metallic, and on some photographic processes, Philos. Trans. R. Soc. Lond. (1840) 1−59.

[2] S.P. Langley, The Bolometer, in Proceedings of The American Metrological Society, vol. 2, 1880, pp. 184-190.

[3] D. Perpetuini, C. Filippini, D. Cardone, A. Merla, An overview of thermal infrared imaging-based screenings during pandemic emergencies, Int. J. Env. Res. Public. Health 18 (6) (2021) 3286.

[4] S. Soldan, On the extended depth of field to improve the quality of automated thermographic measurements in unknown environments, Quant. Infrared Thermogr. J. 9 (2) (2012) 135−150.

[5] C. Ibarra-Castanedo, "Quantitative Subsurface Defect Evaluation by Pulsed Phase Thermography: Depth Retrieval with the Phase," Ph.D. Thesis, Université Laval, 2005.

[6] F.P. Incropera, D.P. DeWitt, T.L. Bergman, A.S. Lavine, Fundamentals of Heat and Mass Transfer, Wiley, New York, 1996.

[7] M. Vollmer, K. Möllmann, Infrared Thermal Imaging: Fundamentals, Research and Applications, John Wiley & Sons, 2017.

[8] N. Ida, N. Meyendorf, Handbook of Advanced Nondestructive Evaluation, Springer International Publishing, 2019.

[9] X.P. Maldague, Nondestructive Evaluation of Materials by Infrared Thermography, Springer Science & Business Media, 2012.

[10] R. Shrestha, W. Kim, Non-destructive testing and evaluation of materials using active thermography and enhancement of signal to noise ratio through data fusion, Infrared Phys. Technol. 94 (2018) 78−84.

[11] I. Garrido, S. Lagüela, R. Otero, P. Arias, Thermographic methodologies used in infrastructure inspection: a review—post-processing procedures, Appl. Energy 266 (2020) 114857.

[12] Y. Chung, R. Shrestha, S. Lee, W. Kim, Thermographic inspection of internal defects in steel structures: analysis of signal processing techniques in pulsed thermography, Sensors 20 (2020) 6015.

[13] R. Shrestha, W. Kim, Evaluation of coating thickness by thermal wave imaging: a comparative study of pulsed and lock-in infrared thermography−Part I: simulation, Infrared Phys. Technol. 83 (2017) 124−131.

[14] Quality Magazine. (2013, July 5). Active Thermography for Nondestructive Composites Testing. Retrieved from https://www.qualitymag.com/articles/91207-active-thermography-for-nondestructive-composites-testing (accessed on 27 April 2023).

[15] R. Shrestha, M. Choi, W. Kim, Thermographic inspection of water ingress in composite honeycomb sandwich structure: a quantitative comparison among lock-in thermography algorithms, Quant. Infrared Thermogr. J. 18 (2021) 92−107.

[16] J. Peeters, G. Steenackers, S. Sfarra, S. Legrand, C. Ibarra-Castanedo, K. Janssens, G. Van der Snickt, IR reflectography and active thermography on artworks: the added value of the 1.5−3 Mm band, Appl. Sci. 8 (2018) 50.

[17] X.P.V. Maldague, Theory and Practice of Infrared Technology for Nondestructive Testing, John Wiley & Son, New York, 2001.

[18] Y. Wei, L. Ding, Y. Han, Y. Luo, Z. Su, D. Zhang, Characterizing defects in materials with fusion of thermography and shearography, Measurement (2021) 109736.

[19] L. Maio, V. Memmolo, S. Boccardi, C. Meola, F. Ricci, N. Boffa, et al., Detection of a defect in a multilayered composite plate, Procedia Eng. 167 (2016) 71−79.

[20] T. Rellinger, P. Underhill, T. Krause, D. Wowk, Combining eddy current, thermography and laser scanning to characterize low-velocity impact damage in aerospace composite sandwich panels, NDT E Int 120 (2021) 102421.

[21] C.A. Larsen, Document Flash Thermography, Utah State University, 2011.

[22] R. Hidalgo-Gato García, J.R. Andrés Álvarez, J.M. López Higuera, F.J. Madruga Saavedra, Quantification by signal to noise ratio of active infrared thermography data processing techniques, Opt. Photonics J 3 (2013) 20−26.

[23] Y. He, B. Deng, H. Wang, L. Cheng, K. Zhou, S. Cai, et al., Infrared machine vision and infrared thermography with deep learning: a review, Infrared Phys. Technol. (2021) 103754.

[24] S.J. Pan, Q. Yang, A survey on transfer learning, IEEE Trans. Knowl. Data Eng 22 (10) (2010) 1345−1359.

[25] M. Wang, W. Deng, Deep visual domain adaptation: a survey, Neurocomputing 312 (2018) 135−153.

[26] A. Kwasniewska, J. Ruminski, M. Szankin, M. Kaczmarek, Super-Resolved Thermal imagery for high-accuracy facial areas detection and analysis, Eng. Appl. Artif. Intell. 87 (2020) 103263.

[27] D. Xu, Y. Wang, S. Xu, K. Zhu, N. Zhang, X. Zhang, Infrared and visible image fusion with a generative adversarial network and a residual network, Appl. Sci. 10 (2020) 554.

[28] H. Zhang, P. Casaseca-de-la-Higuera, C. Luo, Q. Wang, M. Kitchin, A. Parmley, J. Monge-Alvarez, "Systematic infrared image quality improvement using deep learning based techniques", Remote Sensing Technologies and Applications in Urban Environments: International Society for Optics and Photonics (2016).

[29] Almasri, F.; Debeir, O. Multimodal Sensor Fusion In Single Thermal image Super-Resolution. In Asian Conference on Computer Vision; Springer: Cham, Switzerland, 2018; Volume 11367, pp. 418−4

[30] C. Hu, Y. Duan, S. Liu, Y. Yan, N. Tao, A. Osman, et al., LSTM-RNN-based defect classification in honeycomb structures using infrared thermography, Infrared Phys. Technol. 102 (2019) 103032.

[31] Y. Cao, Y. Dong, Y. Cao, J. Yang, M.Y. Yang, Two-stream convolutional neural network for non-destructive subsurface defect detection via similarity comparison of lock-in thermography signals, NDT E Int 112 (2020) 102246.

[32] J. Yang, W. Wang, G. Lin, Q. Li, Y. Sun, Y. Sun, Infrared thermal imaging-based crack detection using deep learning, IEEE Access. 7 (2019) 182060−182077.

[33] J. Hu, W. Xu, B. Gao, G.Y. Tian, Y. Wang, Y. Wu, et al., Pattern deep region learning for crack detection in thermography diagnosis system, Metals 8 (2018) 612.

[34] N. Saeed, N. King, Z. Said, M.A. Omar, Automatic defects detection in CFRP thermograms, using convolutional neural networks and transfer learning, Infrared Phys. Technol. 102 (2019) 103048.

[35] Q. Luo, B. Gao, W.L. Woo, Y. Yang, Temporal and spatial deep learning network for infrared thermal defect detection, NDT E Int 108 (2019) 102164.

[36] W.G. Rieder, Simulation and Modeling, in: R.A. Meyers (Ed.), Encyclopedia of Physical Science and Technology (Third Edition), Academic Press, New York, 2003, pp. 815−835.

[37] A.O. Tapia, R.I. Tsonchev, M. Hern, Modeling of active thermography through uncertainty quantification of parameters of the heat transfer equation, Ann. Math Phys. 2 (2019) 051−057.

[38] W.A. Menner, Introduction to modeling and simulation, Johns. Hopkins APL. Tech. Dig 16 (1995) 6−17.

[39] R. Shrestha, W. Kim, Modelling of pulse thermography for defect detection in aluminium structures: assessment on reflection and transmission measurement, World J. Model. Simul 13 (2017) 45−51.

[40] R. Shrestha, Y. Chung, W. Kim, Wavelet transform applied to lock-in thermographic data for detection of inclusions in composite structures: simulation and experimental studies, Infrared Phys. Technol. 96 (2019) 98−112.

[41] R. Shrestha, S. Sfarra, S. Ridolfi, G. Gargiulo, W. Kim, A Numerical−thermal−thermographic NDT evaluation of an Ancient Marquetry integrated with x-ray and XRF surveys, J. Therm. Anal. Calorim. (2021) 1−15.

[42] R.C. Tighe, J.M. Dulieu-Barton, S. Quinn, Identification of kissing defects in adhesive bonds using infrared thermography, Int. J. Adhes. Adhes 64 (2016) 168−178.

[43] ISO, ISO/TC 135/SC 8—Thermographic Testing, 2021.

[44] ISO, ISO 10878:2013—Non-Destructive Testing—Infrared Thermography—Vocabulary, 2021.

[45] ISO, ISO 10880:2017—Non-Destructive Testing—Infrared Thermographic Testing—General Principles, 2021.

[46] ISO, ISO 18251-1:2017—Non-Destructive Testing—Infrared Thermography—Part 1: Characteristics of System and Equipment, 2021.

[47] ISO, ISO 22290:2020—Non-Destructive Testing—Infrared Thermographic Testing—General Principles for Thermoelastic Stress Measuring Method, 2021.

[48] ISO, ISO 18434-1:2008—Condition Monitoring and Diagnostics of Machines—Thermography—Part 1: General Procedures, 2021.

[49] ISO, ISO 18434−2:2019—Condition Monitoring and Diagnostics of Machine Systems—Thermography—Part 2: Image Interpretation and Diagnostics, 2021.

[50] ISO 18436−7:2014—Condition Monitoring and Diagnostics of Machines—Requirements for Qualification and Assessment of Personnel—Part 7: Thermography, 2021.

[51] ISO, ISO 9712:2012—Non-Destructive Testing—Qualification and Certification of NDT Personnel, 2021.

[52] M. Moradi, S. Sfarra, Rectifying the emissivity variations problem caused by pigments in artworks inspected by infrared thermography: a simple, useful, effective, and optimized approach for the cultural heritage field, Infrared Phys. Technol. 115 (2021) 103718.

[53] M. Moradi, M.S. Safizadeh, Experimental and numerical study of the effect of using polyurethane instead of Teflon strip to simulate debonding defect in composite patch repairs aluminum plate under thermography inspection, Compos. Part. B: Eng. 175 (2019) 107176.

[54] M. Moradi, M.S. Safizadeh, Detection of edge debonding in composite patch using novel post processing method of thermography, NDT E Int 107 (2019) 102153.

[55] G. Poelman, S. Hedayatrasa, J. Segers, W. Van Paepegem, M. Kersemans, An experimental study on the defect detectability of time-and frequency-domain analyses for flash thermography, Appl. Sci. 10 (2020) 8051.

[56] G. Poelman, S. Hedayatrasa, J. Segers, W. Van Paepegem, M. Kersemans, Adaptive spectral band integration in flash thermography: enhanced defect detectability and quantification in composites, Compos. Part. B: Eng. 202 (2020) 108305.

[57] L. Cai, Y. Li, Anomaly detection in thermal images using deep neural networks, in: 2017 IEEE International Conference on Image Processing (ICIP), Beijing, China, 2017, Available from https://doi.org/10.1109/ICIP.2017.8296962.

[58] B. Hu, B. Gao, W.L. Woo, L. Ruan, J. Jin, Y. Yang, et al., A lightweight spatial and temporal multi-feature fusion network for defect detection, IEEE Trans. Image Process 30 (2020) 472−486.